Journal of Science and Technology in Civil Engineering, HUCE (NUCE), 2022, 16 (4): 30–43

PREDICTION OF REINFORCED FLY ASH CONCRETE COLUMNS' BEHAVIOR UNDER ECCENTRIC LOADS USING GAUSSIAN PROCESS REGRESSION

Dang Viet Hung[a], Sykampha Vongchith[a], Nguyen Truong Thang[a,*]

[a]*Faculty of Building and Industrial Construction, Hanoi University of Civil Engineering, 55 Giai Phong road, Hai Ba Trung district, Hanoi, Vietnam*

Article history:
Received 06/6/2022, Revised 25/7/2022, Accepted 22/8/2022

Abstract

Fly ash has been increasingly utilized in concrete industry owing to its advantages in improving workability of fresh concrete and some properties of harden concrete, reducing material cost and adapting sustainable construction requirements. This article introduces a Gaussian process regression using machine learning approach to predict the behavior of reinforced fly ash concrete (RFAC) columns in the form of axial load (N) - mid-height lateral displacement (Δ) relation curve. A dataset collected from an experimental study conducted by the authors and checked to be in accordance with TCVN 5574:2018, is used to train the model with the ratio of 10%. Once being well validated by the remaining 90% of the dataset, it is shown that the model is capable of predicting the N-Δ curves so that the behavior of the tested RFAC columns when subjected to various levels of load eccentricity can be observed and the ultimate resistance of the columns under such condition can be determined.

Keywords: fly ash; column; structure; behavior; second order; machine learning.

https://doi.org/10.31814/stce.nuce2022-16(4)-03

1. Introduction

Fly ash (FA) is a by-product of coal combustion, which is mostly produced from electric power plants. This material can be used as a partial mass replacement of ordinary Portland cement (OPC) to compensate this expensive component of concrete. The use of fly ash in concrete industry is increasing owing to its advantages in improving some properties of concrete, lowering material cost and adapting sustainable construction requirements. Thanks to its pozzolanic and cementitious properties, fly ash contributes to the performance improvement of fresh concrete and the strength gain of hardened concrete [1]. Hence, fly ash can be introduced either as a separately batched material - a mineral additive to reduce the high temperature occurred by hydration reaction in mass-concrete structures - or as a component of blended cement in reinforced concrete structures [1, 2]. Fig. 1 illustrates the applications of fly ash concrete in water damp and infrastructures.

In building structural systems, columns are the critical vertical elements carrying loads from slabs and beams of upper floors to the lower levels and foundations [3–5]. Therefore, columns are primarily compression members with or without eccentricities and will be influenced by slenderness [3–9].

*Corresponding author. *E-mail address:* thangnt2@huce.edu.vn (Thang, N. T.)

Figure 1. Application of fly ash concrete

Although second-order effect was experimental investigated on the behavior of slender reinforced concrete (RC) columns subjected to eccentricities in a number of studies [10, 11], tests conducted on reinforced concrete columns made of fly ash concrete, so-called RFAC columns, were mostly on stocky specimens [12, 13].

(a) Column test by Cross et al. [12]

(b) Column test by Yoo et al. [13]

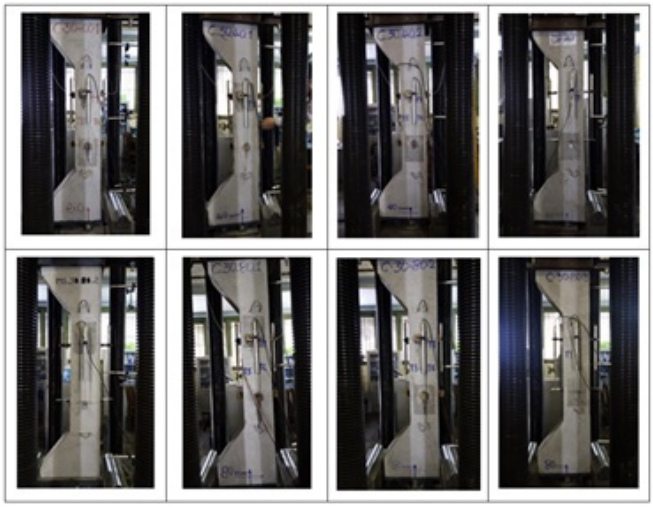

(c) Column test by the authors [14]

Figure 2. Experiments on RFAC columns [12–14]

Cross et al. [12] tested RFAC columns by applying concentric compression load until failure. The column specimens had round cross-section of 152 mm in diameter and 457 mm height. It was shown that the design procedure for RC columns following ACI 318-16 [6] can also be applied for RFAC columns using 15-30% FA/OPC by-mass replacement ratio since the tested columns' behavior is similar to that of OPC columns (Fig. 2(a)). In the experiment conducted by Yoo et al. [13], hi-volume fly ash concrete (HVFAC) with FA/OPC by-mass replacement ratio of 50% was applied for six column specimens. The columns were stocky (Fig. 2(b)) and were concentrically compressed until failed with the resistance lower than that of RC column by 14%. It was shown that the ACI calculation method for RC columns [6] can also be applied for HVFAC columns as the failure criteria of the tested specimens were similar to that of RC columns. The lack of experimental studies on slender RFAC columns subjected to eccentricities motivated the authors to test three groups of eight columns made of fly ash [14]. All the test specimens had identical geometric properties of 150×200 mm rectangular cross-section and 1.6 m-height. Two ends of the specimen were designed with larger dimensions of 150×400 (in mm) to accommodate the uniaxial eccentricities of 0, 40, and 80 mm that are parallel to the longer side of the column cross-section (Fig. 2(c)). Hence, the behavior of RFAC columns incorporated second-order effect could be obtained from the tests in the form of axial load - mid-height lateral displacement relationship [14].

Since it is costly and time consuming to design, prepare and conduct experiments, alternative approaches are also adopted in the research of concrete structures, among which machine learning is a modern technology having high-dimensional nonlinear computing capabilities, intelligent comprehensive analysis and judgment functions, self-learning knowledge reserve expression functions and have been sufficiently applied in various aspects of structures [15–18].

To the best of the authors' knowledge, though there are a number of works studying the fly-ash concrete properties, this work is one of few attempts to investigate the RFAC column behavior under eccentric loads. Moreover, no related database is available in literature at the time of conducting this study. Thus, it is difficult to provide an exact predictive method for the RFAC column; that is why a probabilistic approach is resorted to in this study. In this research, Gaussian Process regression is introduced as a machine learning approach to be effectively applied to predict the RFAC columns' behavior based on the limit dataset obtained from experiments [14]. It is shown that the proposed model after being trained and validated is capable of testing the axial load - mid-height lateral displacement curves with other levels of load eccentricities that were not able to be incorporated in the experimental study.

2. Behavior of RC columns under eccentric loads

In real situations, due to architectural arrangements, unequal column grid-lines, lateral actions (such as wind pressure and ground shaking during earthquakes), column position, construction imperfection, and the reduced column cross-section at upper floors, most columns are subjected to bending about two principal axes, so-called biaxially-loaded columns. In another case such as plane frames in industrial buildings, bending moment about the minor axis is significantly smaller than that about the major axis. For simplicity, the smaller bending moment is often neglected. Single-axis bending about either the major or the minor axis of the column cross-section is termed as uniaxial bending. In the case of braced high-rise buildings, bending moments of columns at lower floors can be significantly smaller than axial force so as they can be ignored in simplified analysis, resulting in pure compression or axially-loaded columns.

Consider three pin-ended columns having the same cross-section properties and are subjected to an axial load N with the same eccentricity e at both ends, so-called the first-order eccentricity. As the columns bend in single curvature under such an applied load, the most critical section is located at the column mid-height. The three columns have different lengths. Column No. 1 has the shortest length l_1 with the smallest slenderness (which is the ratio between the effective length l_1 and the inertia radius r of the cross section) while No. 3 is the longest and most slender column with length l_3. Regardless of their lengths, the interaction diagrams at the critical cross-sections of the three columns can be considered the same (Fig. 3(d)).

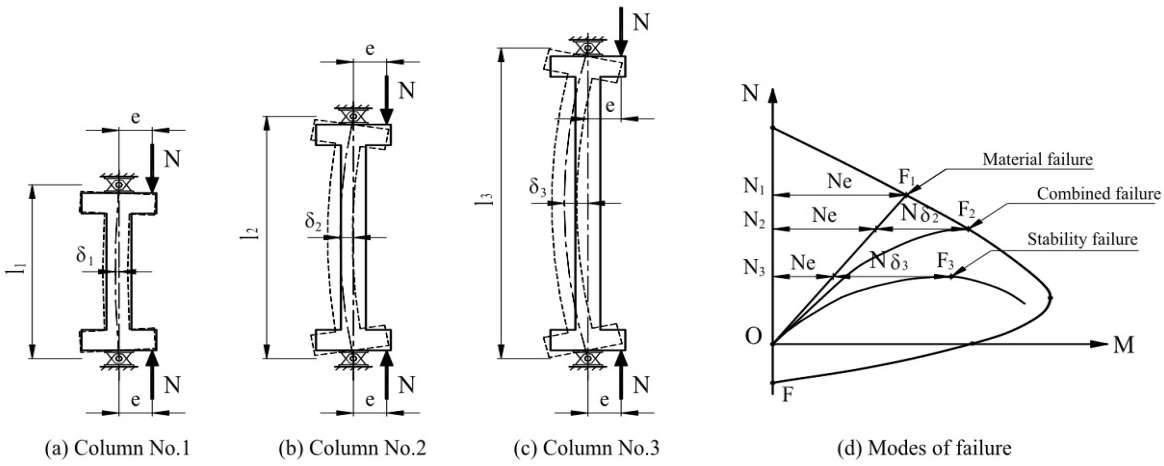

Figure 3. Behaviour of short and slender columns under eccentric load

The structural behaviour of the three columns subjected to gradually-increasing-from-zero axial load N is illustrated in Fig. 3. Under the same value of axial load N, due to their different slenderness ratios, column No. 1 sustains the smallest mid-height lateral deformation while column No. 3 reaches the most. Those lateral deformations are considered as additional eccentricities during the test.

In the case of column No. 1, since the additional eccentricity δ_1 is small, it can be neglected. Thus, the bending moment M equals to Ne at all stages, providing a linear load-moment OF_1 path. Failure occurs when the path reaches the interaction diagram at point F_1, indicating the material failure mode in the extreme compressed concrete fibre. This column then can be considered as a short column.

For columns No. 2 and No. 3, since the additional eccentricities δ_i at their critical cross-sections cannot be ignored, the maximum bending moments M_i is equal to $N(e + \delta_i)$. These P-δ induced moments cause an increase in lateral deflections, which in turn lead to an increament in the moments, resulting in non-linear paths. Then, both the columns can be considered as slender columns. For column No. 2 which has a moderate length, material failure occurs when the non-linear curve OF_2 intersects with the interaction diagram at point F_2, but at a lower failure load N_2, compared to that of column No. 1. For column No. 3 which is very slender, due to its significant lateral deflection, the bending moment increases so rapidly that at a certain deformation δ_3, the value of the derivation $\partial M/\partial N$ approaches infinity before becoming negative, so that the moment resistance reduces with further deflections. When this occurs, the column becomes unstable, resulting in stability failure. At this failure point F_3, the critical load N_3 is smaller than the failure load N_2. It is noted that for column No. 2, if the failure load N_2 is still lower than its stability critical load, the material failure occurs before the stability failure takes place. When these two phenomena happen simultaneously, the

combined failure is said to be occurred.

It can be shown that for slender columns, there is significant reduction in the axial load resistance due to additional moments resulting from pronounced lateral deflections. As shown in Fig. 4(a), due to the *P-δ* effect, the moment is magnified so that point A_1 is shifted to B_1. Alternatively, the interaction curve itself can incorporate the *P-δ* effect by shifting from B_1 back to A_1. As a result, the interaction diagram of slender columns is smaller than that of short columns (Fig. 4(b)).

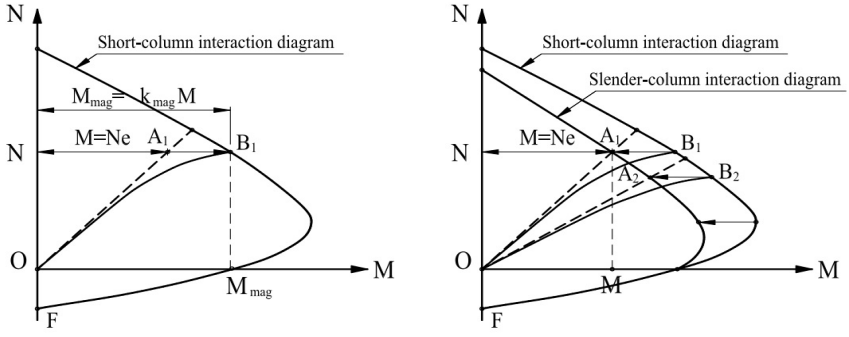

(a) Magnified moment (b) Slender-column interaction diagram

Figure 4. Interaction diagrams of slender columns

3. Experimental results on RFAC columns [14]

In the experimental program conducted by the authors [14], the RFAC column specimens were based on 30 MPa cylinder compressive strength control concrete and were labeled by eccentricities of 0, 40 and 80 mm, which were C-30-00, C-30-40 and C-30-80, respectively. There were 8 specimens distributed in the order of 2:3:3 in the three test series. They were all pin-connected at both ends in the test. The test results of six columns, namely C-30-00 (No. 1 and No. 2), C-30-40 (No. 1 and No. 2) and C-30-80 (No. 1 and No. 2), were introduced in [14]. In this article, the test results of the remaining two column specimens (C-30-40 No. 3 and C-30-80 No. 4) are also combined for the dataset of Gaussian Process regression (Fig. 5 and Table 1).

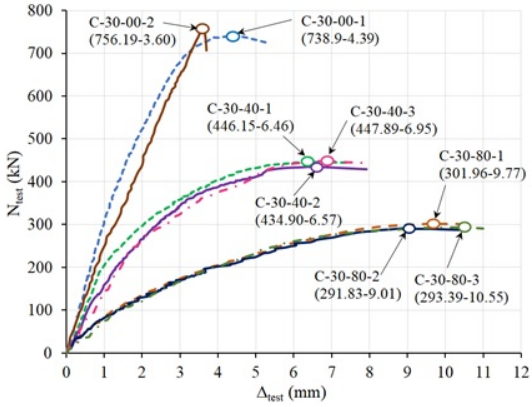

Figure 5. Experimental results on uniaxial load resistance [14]

The experimental relationship between the axial load N_{test} and lateral deflection Δ_{test} at column mid-height measured from all the specimens are shown in Fig. 5, in which the peaks of the curves are also the uniaxial bending resistance of the specimens [14].

It is noted that the initial eccentricity is determined as $e_0 = e_1 + e_a$, where e_1 is the static eccentricity and equals to 0, 40 and 80 mm corresponding to the three groups; e_a is the accidental eccentricity $e_a = \max(L_c/600; h_c/30; 10) = 10$ mm. Hence, the initial eccentricities of the groups C-30-00, C-30-40 and C-30-80 were 10, 50 and 90 mm, respectively. The maximum bending moment at column

mid-height corresponding to the maximum axial load then can be calculated as $M_{test} = N_{test}(e_0+\Delta_{test})$. The calculated values are shown in Table 1. It should be noted that the ratio $(e_0 + \Delta_{test})/e_0$ is also the experimental bending moment magnification ratio.

Table 1. Experimental results on load resistance of RFAC columns [14]

Group	C-30-00 (e_1 = 0)		C-30-40 (e_1 = 40 mm)			C-30-80 (e_1 = 80 mm)		
Specimen	No. 1	No. 2	No. 1	No. 2	No. 3	No. 1	No. 2	No. 3
N_{test} (kN)	738.9	756.19	446.15	434.90	447.89	301.96	291.83	293.39
Δ_{test} (mm)	4.39	3.60	6.46	6.57	6.95	9.77	9.01	10.55
M_{test} (kNm)	10.635	10.288	25.191	24.601	25.505	30.127	28.850	29.500

4. Validation of second-order effect on RFAC columns in [14]

In this section, the second-order effect in terms of moment magnification factor of the tested RFAC columns in [14] will be validated by using TCVN 5574:2018 [9].

The mean compressive strengths measured on 150 mm cubes at 28-day age of groups C-30-00, C-30-40 and C-30-80 were 31.664, 30.890 and 31.704 MPa, respectively. The mean tensile stength of longitudinal rebars was 362.6 MPa. The experimental moduli of elastic for concrete and reinforcing steel were 20.3 and 205 GPa, respectively.

Specimen C-30-80-1 is taken for calculation illustration. It is shown in Table 1 that in the test, this specimen failed at the axial load of N_{test} = 301.96 kN with the corresponding mid-height lateral displacement of Δ_{test} = 9.77 mm.

The column geometrical properties include its cross-section width b = 150 mm and height h = 200 mm; distances from the extreme concrete fiber in compression to the centroidal axes of tensile and compressive longitudinal rebars' cross section are a = 27 mm and a' = 27 mm, respectively, meaning that their distance is z_s = 146 mm; the cross-sectional areas of tensile and compressive rebars (2ϕ14+2ϕ14) are $A_s = A'_s$ = 307.9 mm^2; the effective length of column is L_0 = 1630 mm; the effective depth of column cross section is h_0 = 173 mm; the accidental eccentricity is e_a = max (L_c/600; h_c/30; 10) = 10 mm;

Since the test column is determinate, the initial eccentricity can be calculated as $e_0 = e_1 + e_a$ = 90 mm where the static eccentricity is e_1 = 80 mm. Hence, the relative eccentricity of the axial load is $\delta_e = e/h = 0.45 \in [0.15, 1.5]$. The factor accounting for long-term effect of loading is determined as $\varphi_L = 1 + \dfrac{M_{L1}}{M_L} \leq 2$. Since testing was conducted in a short period of time, one can set $\varphi_L = 1$. Then, the effective factor of cracks in concrete is $k_b = \dfrac{0.15}{\varphi_L(0.3 + \delta_e)} = 0.20$. Moment of inertia of un-cracked concrete in the column cross-section is $I_b = bh^3/12$ = 100,000,000 mm^4. Moment of inertia of longitudinal rebars is $I_s = (A_s + A'_s) \cdot (0.5h - a)^2$ = 3,281,343 mm^4.

As a result, the stiffness of the whole column cross section at ultimate limit states is $D = k_b E_b I + 0.7 E_s I_s$ = 8.775E + 11 Nmm^2.

The conventional critical axial load is $N_{cr} = \dfrac{\pi^2 D}{L_0^2}$ = 3,259,703 N.

Then, the analytical moment magnification factor is $\eta = \dfrac{1}{1 - N/N_{cr}}$ = 1.102 where $N = N_{test}$ =

301.96 kN. The experimental moment magnification factor is. $\eta_{test} = (e_0 + e_{test})/e_0 = 1.109$. Hence, the validation factor is $k_\eta = \eta/\eta_{test} = 0.994$.

Table 2 presents the validation results for all the test specimens.

Table 2. Validation results of moment magnification factor

Group	C-30-00 (e_1 = 0)		C-30-40 (e_1 = 40 mm)			C-30-80 (e_1 = 80 mm)		
Specimen	No. 1	No. 2	No. 1	No. 2	No. 3	No. 1	No. 2	No. 3
δ_e	0.15		0.25			0.45		
k_b	0.333		0.273			0.200		
D (Nmm^2)	11.49E+11		10.25E+11			8.775E+11		
N_{cr} (kN)	4,266.745		3,808.993			3,259.703		
η	1.209	1.215	1.133	1.129	1.133	1.102	1.098	1.099
η_{test}	1.439	1.361	1.129	1.131	1.139	1.109	1.100	1.117
k_η	0.840	0.893	1.003	0.998	0.995	0.994	0.998	0.984
Mean (COV)	0.867 (0.037)		0.999 (0.004)			0.992 (0.007)		

As shown in Table 2, the mean values of the three test series C-30-00, C-30-40 and C-30-80 are 0.867, 0.999 and 0.992, respectively, with the corresponding coefficient of variation (COV) of 0.037, 0.004 and 0.007. If the value of φ_L is set to 2, the corresponding mean values are 0.952, 1.050 and 1.023. Hence, with the accuracy within the range of [−13.3%, 5.0%], it is validated that the second-order effect obtained from the tests was in accordance with TCVN 5574:2018 [9].

In the next section, one presents an alternative and complementary approach that not only provides point estimates of axial force but also associates with uncertainty estimation, which cannot be obtained by using the calculation from TCVN 5574:2018. On the other hand, the GP model is a data-driven approach; thus, its performance objectively depends on the RFAC column database under investigation rather than some subjective assumptions which are predefined for general RC beams yet not specialized for RFAC columns.

5. Gaussian Process regression

In this section, a probabilistic machine learning model is developed to predict the force-displacement relationship (N_{tn}-Δ_{tn}) of RFAC columns tested in [14]. Recently, a large number of regression models ranging from simple linear regression to feature-based machine learning models and to over-parameter deep learning models have been developed to predict the performance of concrete-based structural members [19–21]. However, the performance of these models highly depends on the volume and quantity of data because there are a lot of models' parameters to determine. In reality, performing experiments related to structural components is usually tedious and expensive; therefore, the available experimental data are usually limited compared to other applications. Hence, using an over-parameter model for limited data could lead to the overfitting problem, i.e., the model achieves highly accurate results on training data but provide low accuracy on unseen test data.

On the other hand, during experiments, there are uncontrolled process factors such as environmental conditions, lab technician skills, device sensibility, etc. Thus, two experimental series with exactly the same inputs still yield more or less different results, i.e., one input various outputs. Thus, it is desirable to estimate the uncertainty of obtained results. One of the practical ways is to resort

to probabilistic models such as Bayesian neural network, Dropout-based neural network, Gaussian Mixture model, Gaussian Process, etc. Among these models, Gaussian Process has lower model complexity than deep probabilistic neural network-based models, i.e., there are significantly fewer model parameters to be determined. It neither requires sophisticated theory such as Bayesian probability, Variational Inference nor introduces additional problem-specific hyper-parameter such as Dropout rate, number of layers, and number of neurons. For these reasons, one selects a quasi non-parameter machine learning model, namely, the Gaussian Process (GP) model [22], as the regression model for this study.

Given a set of observed data including inputs $X_1, X_2, \ldots, X_N$ and their respective outputs $Y_1, Y_2, \ldots, Y_N$, the backbone idea of the GP model is that the more similar two inputs X_i and X_j, the more correlated the outputs Y_i and Y_j. The Gaussian Process assumes the probability of an output Y by a multivariate Gaussian distribution:

$$p(Y \mid X, W) = N(\mu, \Sigma) \tag{1}$$

where W is the parameters of GP, μ is the vector of mean value and $\Sigma \in R^{N \times N}$ is the covariance matrix, $\Sigma\left(X_i, X_j\right)$ is used to measure the similarity of inputs, it has three following properties: (i) positive semi-definite $\Sigma\left(X_i, X_j\right) \geq 0$, (ii) achieving maximum value when $X_i = X_j$, i.e., $\Sigma\left(X_i, X_j\right) \leq \Sigma\left(X_i, X_i\right)$ with every X_j, and (iii) symmetric, i.e., $\Sigma\left(X_i, X_j\right) = \Sigma\left(X_j, X_i\right)$.

One of the most adopted kernels is the squared exponential function whose formula for 1-dimensional input is written as below:

$$\Sigma_{SE}\left(X_i, X_j\right) = \sigma^2 \exp\left(-\frac{\left(X_i - X_j\right)^2}{2\lambda^2}\right) \tag{2}$$

where σ is the variance, λ is the length scale. A small value of λ means that the kernel function changes quickly with increasing distance between X_i and X_j, while a large value of λ mean a slow rate of change. The variance σ indicates the variation of the function, which corresponds to the width of the bell shape of the function as shown in Fig. 6.

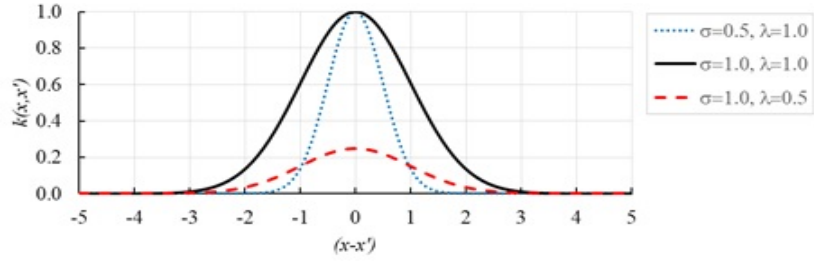

Figure 6. Squared exponential kernels with different values of σ and λ

Because the input X_i for the investigated problem is multidimensional; thus the original squared exponential function is expanded to the additive squared exponential function, which is the sum of individual squared exponential function as follows:

$$\Sigma_{SE}\left(X_i, X_j\right) = \sum_{k=1}^{D} \sigma_k^2 \exp\left(-\frac{\left(X_i^k - X_j^k\right)^2}{2\lambda_k^2}\right) \tag{3}$$

Hence, the hyper-parameters to determine of the GP model are $W = [\sigma_1, \ldots, \sigma_D, \lambda_1, \ldots, \lambda_D]$. In general, the number of available data samples is significantly greater than the number of hyper-parameter that is two dimensional; that is why GP is classified into the quasi-non-parameter family of methods. Next, W is determined by maximizing the log marginal likelihood function which is written by:

$$\log p(Y \mid X, W) = -\frac{1}{2} Y^T \Sigma_{SE}^{-1} Y - \frac{1}{2} \log |\Sigma_{SE}| - \frac{n}{2} \log(2\pi) \tag{4}$$

where n is the number of observed data. The minimum value of $\log p(Y \mid X, W)$ is obtained by setting its gradient to zero as below:

$$\frac{\partial \log p(Y \mid X, W)}{\partial W} = 0 \tag{5}$$

After determining W and Σ_{SE}, one can use the GP model to calculate the output for new input data by:

$$\begin{bmatrix} Y^* \\ Y \end{bmatrix} = \mathcal{N}\left(\begin{bmatrix} \mu_{Y^*} \\ \mu_Y \end{bmatrix}, \begin{bmatrix} \Sigma_{SE}(X, X) & \Sigma_{SE}(X, X^*) \\ \Sigma_{SE}(X, X^*) & \Sigma_{SE}(X^*, X^*) \end{bmatrix} \right) \tag{6}$$

where X and X^* are the observed and input data, while Y and Y^* are the outputs of the observed data and the new input data, respectively.

In short, the implementation steps of the GP model are summarized, as below:

- Step 1: Randomly initialize the model parameters;
- Step 2: Calculate the covariance matrix squared exponential kernels using observed (training) data per Eq. (3);
- Step 3: Run the model, predict new outputs per Eq. (6) and calculate the LLL loss per Eq. (4);
- Step 4: Compute the gradient of LLL loss with respect to the model parameters;
- Step 5: Perform a step of gradient descent optimization by modifying the parameter by a small amount in the negative direction of gradients;
- Step 6: Repeat steps 2 to 4 until the maximum number of iterations or stopping criteria is met (if applied).

6. Analysis results of Gaussian Process regression

The experimental data obtained from a series of experiments with different values of eccentricity of 0, 40 and 80 mm measured in [14] are structured into a tabular dataset, as exemplified in Table 3.

Table 3. Examples of experimental data of fly ash concrete columns

L (mm)	FA %	Rebar	Stirrup	e_1 (mm)	b (mm)	h (mm)	R_{mean} (MPa)	R_s (MPa)	Δ_{test} (mm)	N_{test} (kN)
1600	20	4D14	D6	0	200	150	31.664	362.6	0.00	0.00
…	…	…	…	…	…	…	…	…	…	…
1600	20	4D14	D6	0	200	150	31.664	362.6	4.39	738.90
1600	20	4D14	D6	40	200	150	30.890	362.6	0.00	375.12
…	…	…	…	…	…	…	…	…	…	…
1600	20	4D14	D6	40	200	150	30.890	362.6	4.64	446.15
1600	20	4D14	D6	80	200	150	31.704	362.6	0.00	00.00
…	…	…	…	…	…	…	…	…	…	…
1600	20	4D14	D6	80	200	150	31.704	362.6	9.77	301.96

It is noted that two last columns of dataset shown in Table 3 are also the coordinates of individual points of the curves shown in Fig. 5. Hence, the table has 1634 rows and 11 columns corresponding to the eccentricity, horizontal displacement at the middle of the column, axial load recorded from the load cell, fly ash replacement, rebar details, column cross-section, concrete and steel strengths. In this study, the GP model is trained to predict the value of axial loads N based on other properties. In order to extend the generality of the GP model in the future study, the GP model is designed to encompass 8 input variables, including the column length, FA replacement percentage, rebar ratio, eccentricity, two cross-section dimensions, concrete compressive strength, and horizontal displacement. Meanwhile, the output under investigation is the predicted axial load. In this study, due to the limitation of experimental data, two input properties that vary from sample to sample are the eccentricity and the horizontal displacement Δ. In addition, the concrete compressive strength is slightly different between sample groups, as shown in Table 3. Other properties are the same for all rows. Note that the intent of keeping these columns with unchanged values is to extend the Gaussian Process in the future to take into account more properties as input, just by appending new data to this table without requiring any modification. Because the GP model has a small number of parameters to determine; thus, only a small part of the dataset serves as training data. Specifically, 10% of the data, i.e., 165 data samples, are randomly selected to train the GP model, and the remaining of 90%, thus 1469 samples are used to validate the final model.

Fig. 7(a) represents the evolution of the log-likelihood loss function on the validation dataset in function of the numbers of learning iterations using a learning rate $\lambda = 0.001$. It can be seen that the loss function steadily decays for the first 400 iterations, then slightly decreases from iteration 400 to iteration 600 before showing a stable trend without clear improvement.

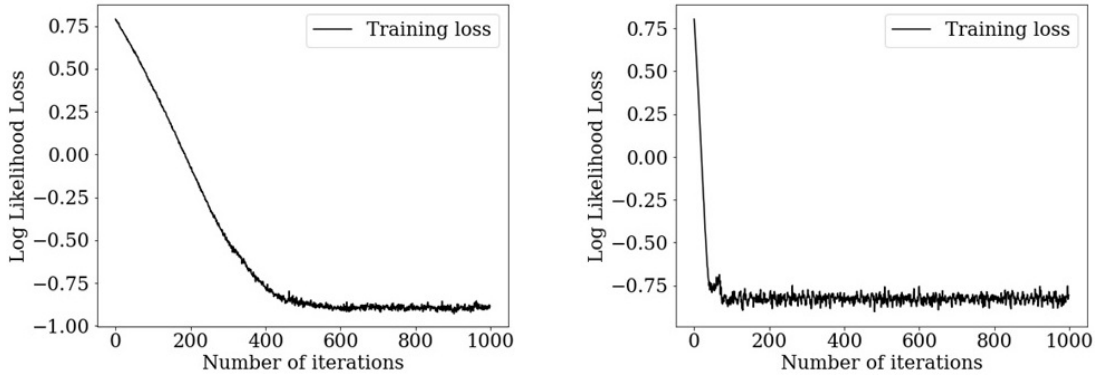

(a) Learning rate $\lambda = 0.001$ (b) Learning rate $\lambda = 0.01$

Figure 7. Evolution of the loss function in function of the number of interations with

It is noteworthy that one of the advantages of the GP model is that it requires significantly less training data than its counterparts. For example, neural network-based methods usually need a major part of data for the training process; only a small number of data is left for validation. Hence, additional technique, such as the K-fold method, is required to ensure the reliability of the model evaluation. Meanwhile, in this study, one uses only 10% of the data for training the GP model, yet up to 90% of data can be used for validating the trained model, as presented above.

To show the impact of the training size on the model performance, Table 4 enumerates the loss function LLL of the training process and other popular evaluation metrics for regression problems

such as the coefficient of determination (R^2), mean absolute value (MAE), and root mean square error (RMSE) on the validation dataset. It can be seen that using 10% of data is enough to provide reasonably accurate results in this study as its measure metrics are slightly higher than other amounts but its CPU times is considerably faster.

Table 4. Influence of training data volume on the training process results

Training data	10%	20%	30%	40%	50%	60%	70%	80%	90%
LLL	−0.83	−0.82	−0.87	−0.87	−0.88	−0.84	−0.87	−0.88	−0.89
R2	0.98	0.98	0.98	0.98	0.99	0.99	0.99	0.99	0.99
MAE	10.59	10.58	10.50	10.40	10.36	10.31	10.27	10.08	10.04
RMS	15.78	15.57	15.55	15.47	15.39	15.21	15.03	14.98	14.86
CPU time (s)	7.6	14.2	32.3	40.6	52.1	70.5	98.8	126.3	158.1

To clearly show the performance of the learned model, Fig. 8 presents the comparison results between the predicted axial loads and the experimental ones for the training dataset. In the figure, the 45-degree red line denotes an ideal scenario of perfect agreement between prediction and experimental results, while for each scattered dot, its abscissa and ordinate are the experimental and the predicted values, respectively. As expected, scatter dots closely lie to the ideal line; these dots are apparently equally distributed on two sides of the line, implying that the predicted results are not biased.

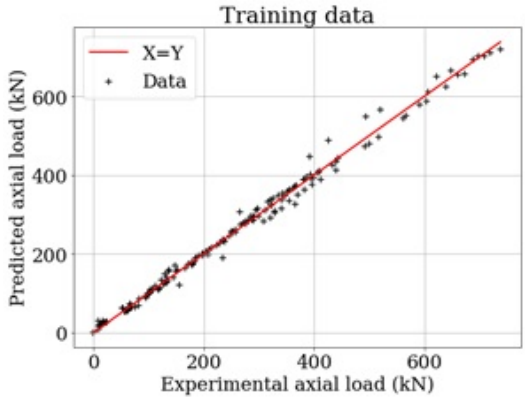

Figure 8. Comparison results between GP model and experiments on training data

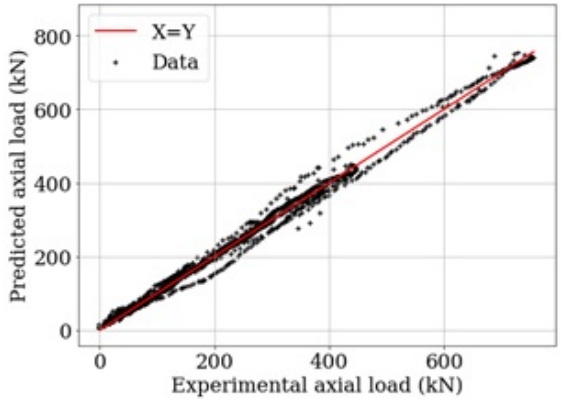

Figure 9. Comparison results between GP model and experiments on testing data

A similar agreement is obtained on unseen testing data with significantly more samples as shown in Fig. 9.

Quantitatively, Fig. 10 depicts a histogram of relative errors in percentage between predicted results and experimental ones, the errors have a mean of 1.06% and a standard value of 7.4%.

Figs. 11, 12 and 13 represent the N-Δ relation curves reconstructed by using the GP models. Note that the predictions are repeated 100 times, then the mean values (solid blue line) and the 2σ-interval, a.k.a, 95%-confidence interval area (gray shaded area) are derived. Obviously, almost all experimental data are encompassed within the 95% CI, which reaffirms the viability of the Gaussian Process. In

terms of the inference time, it takes only 256 ms to perform about 1469 test samples, i.e., about 25s in total for repeating 100 times the inference.

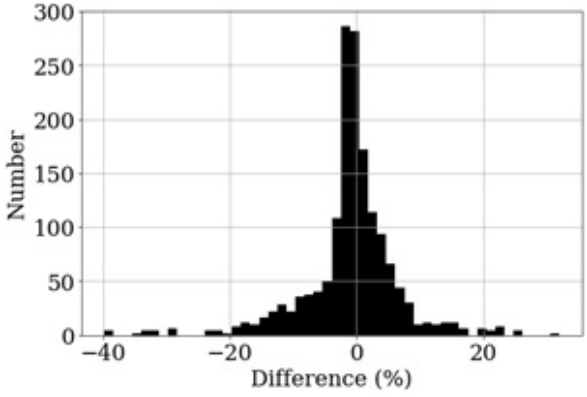

Figure 10. Histogram of relative differences between GP model and experiments

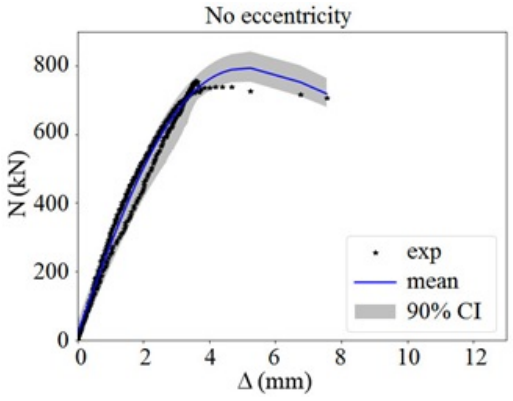

Figure 11. The N-Δ relation curves curves reconstructed by GP model for $e_1 = 0$

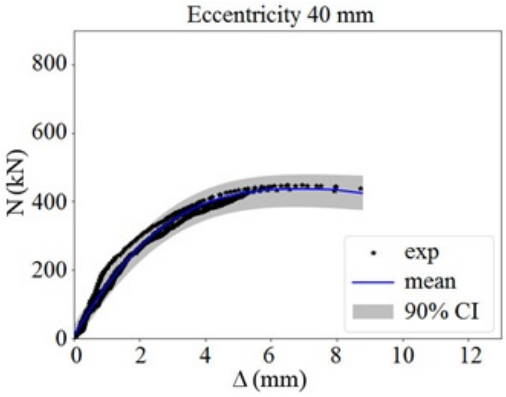

Figure 12. The N-Δ relation curves reconstructed by GP model for $e_1 = 40$ mm

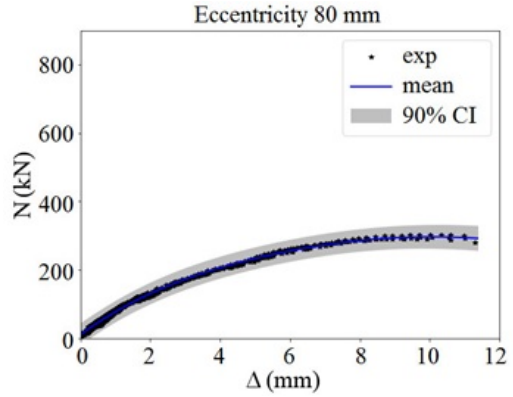

Figure 13. The N-Δ relation curves reconstructed by GP model for $e_1 = 80$ mm

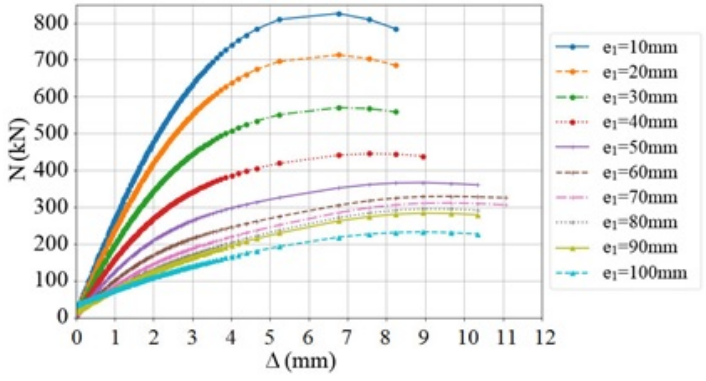

Figure 14. The N-Δ relation curves predicted by GP model

Recall that experimental data are only available for eccentricities of 0, 40, and 80 mm. Therefore, the validated GP is used to derive the N-Δ relation curves for other values of eccentricity from 10 to 100 mm as shown in Fig. 14.

The axial load - mid-height lateral displacement relation curves depicted in Fig. 14 provide an explicit strengthen of the observation from the test results on $e_1 = 0, 40$ and 80 mm that the behavior of RFAC columns under uniaxial load is negatively influenced by the static eccentricity e_1. Furthermore, the ultimate resistance of the investigated specimens can be directly determined from the peak of the curves.

7. Conclusions

A number of conclusions can be withdrawn from the analytical study and machine learning investigation presented in this article as follows:

- There have been limited experimental results of the behavior of reinforced fly ash concrete (RFAC) columns under eccentric loading condition in literature. Hence, it is important to investigate the second-order effect on RFAC columns that is expressed via the axial load (N) - mid-height lateral displacement (Δ) relation curves;

- Based on the N-Δ relation curves measured in the testing program of the authors on a number of eight RFAC column specimens, the second-order effect on the tested RFAC columns is validated to be in accordance with TCVN 5574:2018;

- The Gaussian Process regression introduced in this paper is an efficient regression tool utilizing machine learning approach. After being trained and well validated by the corresponding percentages of 10% and 90% of the dataset collected from the experiment on eight RFAC columns, the proposed model in capable of capturing a larger picture of the behavior that is an overall prediction of the N-Δ relation curves when the test RFAC columns are loaded in various eccentricities.

The results obtained in this paper can be further developed to prove the capability of applying fly ash into concrete industry and structures sufficiently, taking into account the second-order effect on the behavior to predict the resistance of RFAC columns closely and conservatively. For the next step of the study, it is desirable to enrich the RFAC column databases with other eccentricity values, FA replacement ratios, and more geometrical configurations to validate, then adjust the prediction curves in Fig. 14 and to improve the generality of the GP model.

Acknowledgement

This research is funded by Hanoi University of Civil Engineering, Vietnam (HUCE), under grant number 44-2021/KHXD-TD. Technical supports from Laboratory LAS-XD 125 (HUCE) are also appreciated by the authors.

References

[1] ACI 232.2R-18 (2018). *Report on the use of fly ash in concrete*. American Institute of Concrete.

[2] ASTM C618-12a (2012). *Standard specification for coal fly ash raw or calcined natural pozzolan for use in concrete*. West Conshohocken, PA: American Society for Testing and Materials.

[3] Wight, J. K., MacGregor, J. G. (2012). *Reinforced concrete: Mechanics and design*. 6th edition, Pearson Education Inc. Upper Saddle River, New Jersey 07458.

[4] Mosley, B., Bungey, J., Hulse, R. (2007). *Reinforced concrete design to Eurocode 2*. Palgrave MacMillan, New York.

[5] Minh, P. Q., Phong, N. T., Thang, N. T., Tung, V. M. (2021). *Reinforced concrete structures - Basic elements*. Publishing House of Science and Technology (in Vietnamese).
[6] ACI 318-16 (2016). *Building code requirements for structural concrete*. American Institute of Concrete.
[7] EN 1992-1-2:2004 (2004). *Eurocode 2: Design of concrete structures. Part 1-2: General rules - structural fire design*.
[8] SP 63.13330.2012 (2019). *Concrete and reinforced concrete structures - Principal rules*. Ministry of Regional Development of the Russian Federation (in Russian).
[9] TCVN 5574:2018. *Concrete and reinforced concrete structures - Design standard*. Ministry of Science and Technology (in Vietnamese).
[10] Tan, K. H., Nguyen, T.-T., Nguyen, T. T. (2012). *Discussions on using EN 1992-1-1:2004 in design of precast prestressed planks and biaxially-loaded slender columns*. Proceedings of the Third International Workshop on Design of Concrete Structures Using Eurocodes, Viena, pages 203-210.
[11] Tan, K.-H., Nguyen, T.-T. (2013). Experimental behaviour of restrained reinforced concrete columns subjected to equal biaxial bending at elevated temperatures. *Engineering Structures*, 56:823–836.
[12] Cross, D., Stephens, J., Vollmer, J. (2015). *Structural applications of 100 percent fly ash concrete*. World of Coal Ash, Kentucky, USA, 1-19.
[13] Yoo, S.-W., Choi, Y. C., Choi, W. (2017). Compression behavior of confined columns with high-volume fly ash concrete. *Advances in Materials Science and Engineering*, 2017:1–11.
[14] Sykhampha, V., Thang, N. T. (2021). Experimental study on load bearing capacity of reinforced fly ash concrete columns subjected to uniaxial bending. *Journal of Science and Technology in Civil Engineering (STCE) - HUCE*, 15(5V):79–94. (in Vietnamese).
[15] Hu, X., Li, B., Mo, Y., Alselwi, O. (2021). Progress in artificial intelligence-based prediction of concrete performance. *Journal of Advanced Concrete Technology*, 19(8):924–936.
[16] Hung, D. V., Hung, H. M., Anh, P. H., Thang, N. T. (2020). Structural damage detection using hybrid deep learning algorithm. *Journal of Science and Technology in Civil Engineering (STCE) - HUCE*, 14 (2):53–64.
[17] Hung, D. V., Thang, N. T., Dat, P. X. (2021). Probabilistic pushover analysis of reinforced concrete frame structures using dropout neural network. *Journal of Science and Technology in Civil Engineering (STCE) - HUCE*, 15(1):30–40.
[18] Hung, D. V., Thang, N. T. (2022). Predicting dynamic responses of frame structures subjected to stochastic wind loads using temporal surrogate model. *Journal of Science and Technology in Civil Engineering (STCE) - HUCE*, 16(2):106–116.
[19] Tran, V. Q., Dang, V. Q., Ho, L. S. (2022). Evaluating compressive strength of concrete made with recycled concrete aggregates using machine learning approach. *Construction and Building Materials*, 323:126578.
[20] Liang, M., Chang, Z., Wan, Z., Gan, Y., Schlangen, E., Šavija, B. (2022). Interpretable Ensemble-Machine-Learning models for predicting creep behavior of concrete. *Cement and Concrete Composites*, 125:104295.
[21] Shamsabadi, E. A., Roshan, N., Hadigheh, S. A., Nehdi, M. L., Khodabakhshian, A., Ghalehnovi, M. (2022). Machine learning-based compressive strength modelling of concrete incorporating waste marble powder. *Construction and Building Materials*, 324:126592.
[22] Rasmussen, C. E., Williams, C. K. I. (2019). *Gaussian processes for machine learning*. London, England: MIT Press.